Design of a smart morphing wing using integrated and distributed trailing edge camber morphing

Mkhoyan, Tigran; Thakrar, Nisarg Rashmin; de Breuker, Roeland; Sodja, Jurij

Important note
To cite this publication, please use the final published version (if applicable).
Please check the document version above.

SMASIS-2370

DESIGN OF A SMART MORPHING WING USING INTEGRATED AND DISTRIBUTED TRAILING EDGE CAMBER MORPHING

Tigran Mkhoyan
Aerospace Structures and Materials department
Delft University of Technology
Delft, P.O. Box 5058,2600GB
The Netherlands
Email: T.Mkhoyan@tudelft.nl

Nisarg Rashmin Thakrar[*]
Roeland De Breuker [†]**Jurij Sodja** [‡]
Aerospace Structures and Materials department
Delft University of Technology
Delft, P.O. Box 5058,2600GB
The Netherlands 2629 HS

ABSTRACT

In this study, the design and development of an autonomous morphing wing concept were investigated. This morphing wing was developed in the scope of, the Smart-X project, aiming to demonstrate in-flight performance optimisation. This study proposed a novel distributed morphing concept, with six Translation Induced Camber (TRIC) morphing trailing edge modules, interconnected triangular skin segments joined by an elastomer material to allow seamless variation of local lift distribution along the wingspan. An FSI structural optimisation tool was developed, to achieve this optimised design, and to produce an optimal laminate design of glass fibre weave material, capable of reaching target shapes and minimise actuation loads. Analysis of the kinematic model of the embedded actuator was performed, and a conventional actuator design was selected to continuously operate at the required load and fulfil both static and dynamic requirements in terms of bandwidth, actuation force and stroke. Preparations were made in this study for the next stage of the Smart-X design, to refine the morphing mechanism design and build a functional demonstrator for wind tunnel testing.

NOMENCLATURE

ρ	Air Density $[kg/m^3]$
θ_{act}	Actuator Rotation $[°]$
$\theta_{linkage}$	Included angle between F_{act} and $F_{linkage}$ $[°]$
C_L	Coefficient of Lift $[-]$
c_{paero}	Aerodynamic Pressure Coefficient
F_{act}	Actuator Force $[N]$
$F_{linkage}$	Linkage Force $[N]$
F_{react}	Reaction Force at Linkage $[N]$
r_{act}	Torque Arm Length $[m]$
T_{act}	Actuator Torque $[N.m]$
V_∞	Air Speed [m/s]
$c_{P\,fem}$	Aerodynamic Pressure Coefficient interpolated on FEM mesh

ABBREVIATIONS

FEM	Finite Element Model
FSI	Fluid Structure Interaction
TE	Trailing Edge
TRIC	TRailing Edge Induced Camber

---

[*]N.R.Thakrar@student.tudelft.nl,2600GB Delft, The Netherlands
[†]R.DeBreuker@tudelft.nl,2600GB Delft, The Netherlands
[‡]J.Sodja@tudelft.nl ,2600GB Delft, The Netherlands

INTRODUCTION

The advancements in aerospace materials, manufacturing technology, controller and hardware design allow developing increasingly flexible aircraft concepts. Generally, the flexibility

comes as a side effect of lighter aircraft design and needs to be adequately accounted for, however, a more natural approach is to utilise the flexibility for the benefit of better performance, much like the morphing wings found in nature, allowing better gliding performance [1, 2]. As in nature, morphing wing concepts have been evolving since the early years of the aviation. One of the well-documented examples was the active roll control of the Wright Flyer, the first successful heavier-than-air powered aircraft. In this lightweight design, the lateral stability was ensured by wing twist-warping [3], and the flexible fabric-wrapped structure was well suited for morphing. As the flight speeds and loads were increased with the advancement of flight, a stiffer wing was required to fulfil structural requirements and overcome aeroelastic instabilities. As a result, this rigid wing design - generally optimised for the cruise - exhibited compromised performance outside of the optimised cruise conditions. Active morphing is a technology that holds the potential to reduce this performance gap and to improve the aircraft performance across the flight envelope. However, a challenging aspect in active morphing is designing a feasible and effective morphing mechanism, improve aircraft performance across the flight envelope [4]. In literature, various morphing concepts can be found each with their advantages and disadvantages. A comprehensive review of the early morphing concepts is found in [5] various approaches regarding the actuator material, the actuation mechanism, and the skin types. In the latter two categories, examples vary from conventional to compliant mechanisms and materials. Also, various materials are investigated for the actuator, ranging from conventional to piezoelectric or shape memory alloys. The morphing can be applied to the leading edge, trailing edge or both. Kintscher et al. [6] and Sodja et al. [7] investigate seamless morphing droop nose concept for the leading edge, designed to match a given target shape with different materials used (glass-fibre prep-reg and aluminium). The concept by Sodja et al. utilises conventional actuation. Here, low actuation forces are achieved by maintaining the skin length under morphing, such that strains in the skin are kept minimal. Several other concepts [8–10] achieve low actuation force by utilising compliant skin and actuation mechanism. While promising, the studies highlight the importance of further research into manufacturing and up-scaling of complex compliant designs, since the manufacturing process of these complex shapes is still challenging. Further examples of the compliant mechanism are investigated in the literature combined with conventional actuators (Previtali et al.) [9, 11] and piezoelectric skin actuation (Molinari et al.) [10, 12]. Some studies use bio-inspired design, such as the FishBAC concept, designed to mimic the compliant skeletal frame of fish, developed at Swansea University [13–15]. Trailing edge mechanisms are also presented by FlexSys [9, 16], which have been installed and undergone flight test on the Gulfstream business jet [17]. Recent studies also investigated the use of ultralight, lattice-based, structural modules assembled in a modular adaptive structure. The advantage is that these materials can have the stiffness of a typical elastomer at the mass-density typical to aero-gel. Cremer et al. [18] demonstrate improved aerodynamic efficiency and roll control authority with spatially programmed elastic morphing shape of a 4.27 m wingspan aircraft in the wind-tunnel. Jennet et al. [19] present the digital morphing wing concept, constructed from discrete lattice elements. This concept shows increased roll efficiency compared to a conventional wing, by applying span-wise twisting deformation. While promising, due to its programmable flexibility and lightweight, the lattice-based modules occupy the majority of the internal space. Therefore, additional consideration is needed to ensure flexibility of the structure, while reserving the room for fuel, batteries and/or additional components to be installed in the wing. Aside from the internal actuation mechanism, two other studies introduced the concept morphing through direct skin actuation, with piezoelectric actuators (Bilgen et al. [20, 21]) and macro fibre composite actuators for camber morphing (Pankonien et al. [22]). Another wing concept by Mistry et al. [23] demonstrated cross-sectional warping mechanism to realise variable camber on a rotor blade. The literature survey suggests that many morphing concepts are restricted to either twist or camber morphing mechanisms, propose a complex mechanism that introduces manufacturing challenges or consume a large portion of the internal volume. Furthermore, most concepts show global morphing approach, while in the scope of active control, a distributed and over-actuated mechanism is necessary to apply simultaneous load alleviation, flutter suppression and drag minimisation. In a recent study for the EU FP7 CHANGE project, a morphing concept called the Translation Induced Camber (TRIC), is introduced to address some of these problems [24]. This concept implements a relatively simple and effective morphing mechanism that uses a combination of cross-sectional warping and skin bending to induce both camber and twist morphing. This concept has the advantage that conventional actuators can be used due to its relatively simple and compact design, and significant space is reserved inside the main wingbox, for fuel and installation of additional components such as pipes and the auxiliary systems. The main disadvantage of this concept is that the morphing is global across the span and the control is governed by only a pair of actuators (per trailing and leading edge), respectively. This does not allow local control of caber or twist distribution across the span.

To address this problem, the current study extends on the TRIC concept. It introduces a distributed and modular morphing design, with interconnected triangular skin segments joined by an elastomer material to allow seamless variation of local lift distribution along the wingspan. This morphing design was developed in the scope of an autonomous smart wing concept, called the Smart-X wing. This wing concept aims to demonstrate an integrated and coherent approach towards multi-objective load alleviation, flutter suppression and performance optimisation of adaptive aircraft wings.

This paper is structured in the following way. First, the scope of the Smart-X project is presented in 1, then a brief overview of the design evolution of the TRIC concept and the morphing mechanism of the Smart-X morphing concept is presented in Sec. 2. In Sec. 3, the numerical design approach and the methodology behind Fluid-Structure Interaction (FSI) framework, developed as a tool to both design and produce a control ready surrogate model of this concept is discussed. Next, the optimisation methodology and framework is discussed in Sec. 4, leading to the development of a fully composite smart morphing wing with conventional actuator mechanism, presented in Sec. 5. Finally, the conclusions of the design outcome, actuator selection and surrogate model development are presented in Sec. 6.
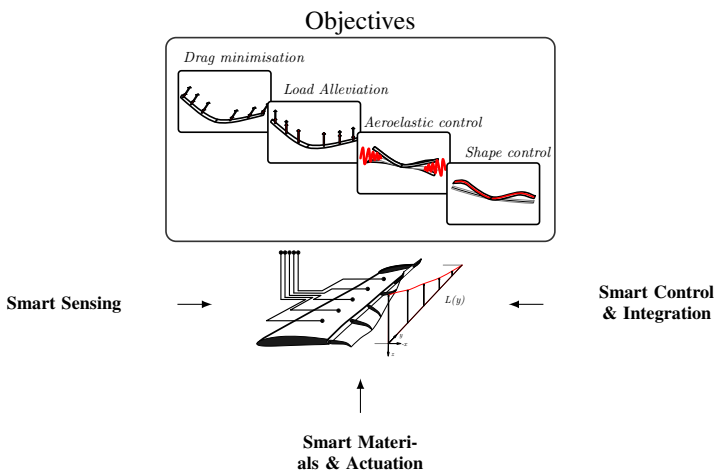
1 SMART-X PROJECT

FIGURE 1: RATIONALE BEHIND THE SMART-X

The problem addressed in the current study was to investigate a morphing concept that would allow span-wise distributed camber morphing, for shape and load alleviation control of an over-actuated and over-sensored composite wing. TRIC concept served as the basis, which leads to the development of a fully composite smart morphing wing concept. The Smart-X wing aims to demonstrate in-flight performance optimisation of multiple objectives such as (i) drag optimisation, (ii) load alleviation, (iii) flutter suppression and (iv) shape control through multidisciplinary utilisation of smart sensing, control, actuation and integration. Fig. 1 presents the rationale behind the integrated design of the Smart-X.

The objectives following from the problem statement can be summarised as follows:

1. Distributed chord-wise morphing along the full span with modular morphing units based on TRIC
2. Ensure span-wise continuity between each morphing module
3. Develop a tool to construct an input-output surrogate model suitable for the assessment of control states and control effectiveness

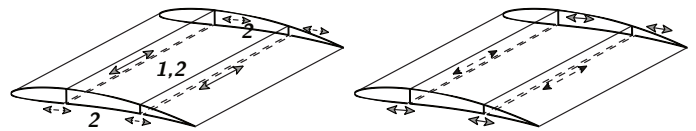## 2 DISTRIBUTED MORPHING TRIC CONCEPT

FIGURE 2: TRIC DESIGN EVOLUTION [24].

The literature survey presented in the previous chapter highlighted some of the shortcomings of the previous morphing designs. The TRIC concept, developed during the CHANGE project, addresses some of these problems [24]. The underlying idea of the TRIC is to implement a combination of cross-sectional warping and skin bending to induce both camber and twist morphing, with the advantage that conventional actuators can be used due to its relatively simple and compact design, and significant space is reserved inside the wing for the instalment of necessary auxiliary components. TRIC concept finds its origin in the work of Vos et al. [25], which introduces a twist morphing concept based on the principle of a warping cross-section. Similar to the concept by Vos et al., TRIC introduces a cut along the span on the bottom of the wing, and uses span-wise actuation, without any chord-wise movement. While this introduces the intended warping of the skin, due to the relatively large stiffness of the win-box, additional shear is introduced in the skin, thereby increasing the required actuation forces, the weight of the mechanism, and introducing non-linearity in twist distribution along the span. From here on, the concept undergoes design evolution in two additional steps, where, in the next step, chord-wise movement is allowed. This greatly reduces the required actuation forces and resulting in linear twist distribution along the span. In the final step, the actuation direction is changed from span-wise to chord-wise, allowing the combined camber and twist morphing. By altering the actuation direction, two sets of actuator working either symmetrically (same direction) or asymmetrically (opposite direction), can introduce pure camber morphing
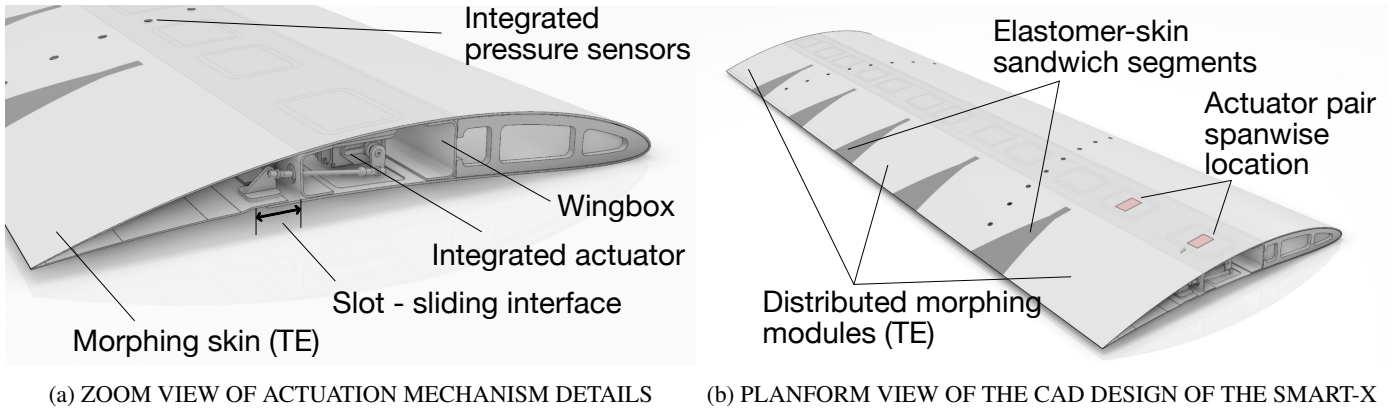
(a) ZOOM VIEW OF ACTUATION MECHANISM DETAILS

(b) PLANFORM VIEW OF THE CAD DESIGN OF THE SMART-X

FIGURE 3: CAD IMPRESSIONS OF THE SMART-X DESIGN

or, warp-induced span-wise twist morphing. An illustration of the design evolution of the TRIC concept is shown in Fig. 2 taken from [24].

In its final stage, the TRIC concept achieves an efficient compact design, where the actuation forces are kept low, and the internal space is not compromised. However, in the scope of smart active control, this concept has the disadvantage that the morphing module, with a single pair of actuators, is global across the span. This implies that no local camber or twist distribution is allowed across the span. However, in the scope of smart integrated multi-objective control, local control of lift coefficient increments and thereby local lift distribution is essential. The current study aims to address this deficiency and further develop the TRIC concept. An integrated autonomous wing concept is proposed, which features distributed trailing edge morphing modules along the span. In the current case, the autonomous wing, includes six such morphing modules based on the TRIC concept, allowing the independent camber and span-wise twist morphing of local span segments. As with the TRIC concept, the skin is actuated internally, allowing smooth and seamless morphing along the chord. The morphing target shape is commanded using high-performance servos embedded in the wing box, allowing the trailing edge bottom skin to slide chord-wise and partly span-wise direction inside a specifically designed slot. This is illustrated in Fig. 3a. An advantage of this design is that the actuator mechanism can also be relocated to the trailing edge section, such that actuation occurs by pushing away from the wing-box. Each module is equipped with two pairs of actuators allowing local symmetric (pure bending) and asymmetric (twist) morphing. Interconnected triangular skin segments, joined by an elastomer material, allow continuous span-wise variation of the lift distribution between the morphing modules. These segments are composed of the skin-elastomer sandwich. This is illustrated in Fig. 3b.

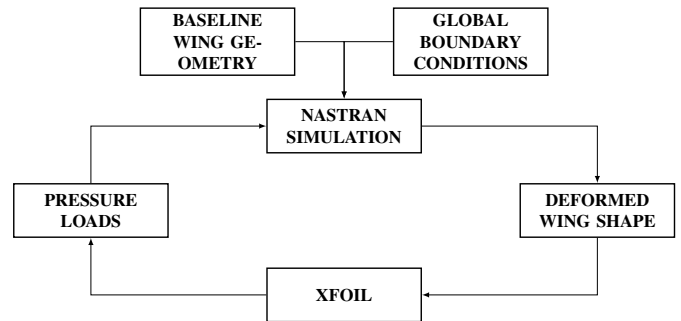The main advantage of the current design is that by adjusting

FIGURE 4: FLOW CHART OF THE FSI FRAMEWORK.

the camber and twist distribution, the lift distribution can be controlled locally and independently for each module, allowing the wing to settle into the most optimal lift to drag ratio (*shape control,*) to *minimze drag*. Furthermore, the lift distribution can be adapted to perform manoeuvre *load alleviation* when necessary. Lastly, fast piezoelectric actuators are placed at the tip of the morphing trailing edge for *aeroelastic control* (e.g. flutter suppression), hereby covering the targets presented earlier in Fig. 1. To sustain the required loads, meet the actuator constraints, and to achieve the desired morphing shapes, the composite wing skin is tailored and optimised. Therefore, a Fluid-Structure Interaction (FSI) structural optimisation tool is developed, that allows for (i) fast analysis and (ii) fast optimisation of ply orientation and thickness in terms of the given input loads, desired target shapes and actuator limits. The applied methodology behind this assessment is presented in the next section.

3 DESIGN METHODOLOGY

To meet the objectives listed in section 1, an FSI tool was developed to connect the Finite Element Model (FEM) and the Aerodynamic model. The tool was developed with two goals in

4

mind, namely, (i) to produce the required morphing design presented in Sec. 2 and (ii) to allow quick assessment of the wing performance under given aerodynamic load and commanded actuators input position, such that a surrogate model of the morphing wing can be built. The surrogate model, extracted from the analysis data, represented input-output mapping of the actuator input versus deflected shape output and the control effectiveness in terms of lift increment needed for real-time active morphing control and achievement of multiple objectives listed in Sec. 1, Fig. 1.
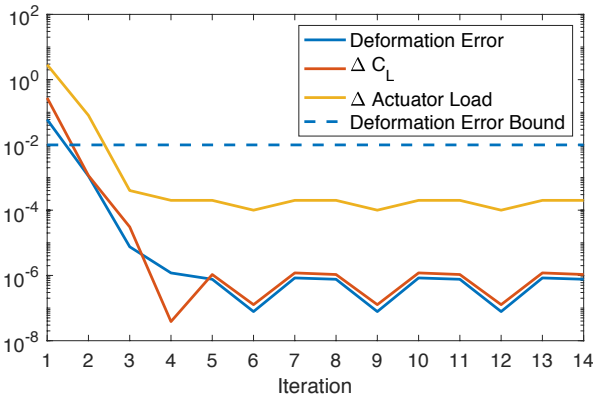

FIGURE 5: FSI LOOP CONVERGENCE.

3.1 FSI Framework

The outline of the FSI framework is illustrated in Fig. 4. The framework couples NASTRAN (Structural) [26] and XFOIL (Aerodynamic) [27] in an analysis loop, with MATLAB, used to interface the two software. For each loop iteration, actuator nodes were displaced, and the deformed shape was extracted from NASTRAN and parsed through XFOIL to extract pressure distribution data. The pressure data was then applied to the NASTRAN mesh as additional pressure loads to the original simulation. The loop was iterated until the deformed shape, and therefore lift, and actuation loads converged. As shown in Fig. 5 convergence of these variables is typically reached in three to four iterations.

3.2 FEM

The FEM model was developed in NASTRAN [26] and consists of a 500mm chord and 300mm span section module with a cut introduced at the bottom skin. The cut is bridged by an actuator pair installed at each end of the module, which serves two purposes: (i) provide symmetric and asymmetric actuation input and (ii) prevent the skin from moving under exerted aerodynamic loads (re-closing the cross-section). The flexible skin is allowed

to slide in the chord-wise and transverse direction to accommodate the required morphing shape under loads. Vertical deformations and rotations about the transverse and chord-wise axis are restrained. Fig 6 shows the boundary conditions employed in the FEM model. These boundary conditions, allowed to perform
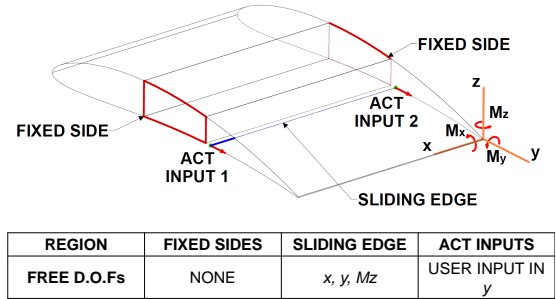

REGION	FIXED SIDES	SLIDING EDGE	ACT INPUTS
FREE D.O.Fs	NONE	x, y, Mz	USER INPUT IN y

FIGURE 6: FEM MODEL BOUNDARY CONDITIONS

the following morphing shapes, which are threaded as morphing sub-cases in the FSI model:

1. Bend up
2. Bend down
3. Twist
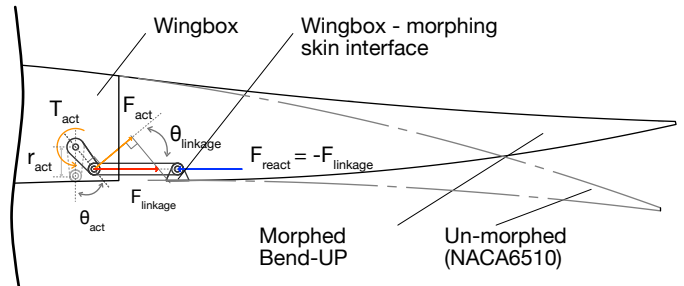
FIGURE 7: FREE BODY DIAGRAM OF THE ACTUATOR MECHANISM

3.2.1 Actuator Model To facilitate the actuator sizing, and the surrogate model capability in terms of actuator input and morphing behaviour, the kinematic model of the actuator and the morphing interface had to be added. Fig. 7 shows (in a cross-sectional view) the FBD (Free-Body Diagram) of the actuator force and moment equilibrium for the bend up case. A typical (immediate) input to the actuator is torque, which results in a

5

commanded servo angle (rotational position). Examining the diagram, two important aspects can be noted regarding the actuator input force to the morphing interface: (i) The maximum actuator force, F_{max} that can be delivered at the attachment on the servo arm will increase by shortening the servo arm r_{act} (ii) The instantaneous actuator torque T_{act} required to balance or overcome the reaction forces at the morphing interface, F_{react}, is not linear for the range of travel of the actuator. The latter aspect results from the kinematic relationship of F_{act}, representing the actuator torque for a given actuator arm r_{act} and the linkage force $F_{linkage}$. Since the F_{act} is a projection of the $F_{linkage}$ on line normal to the servo arm ($F_act < F_{linkage}$), F_act and thus the amount of torque required by the actuator to balance or overcome the reaction forces are dependent on the deflection of the linkage system from of the servo arm.

The relation of linkage force to $\theta_{act,max}$ is presented in Fig 18, and is defined by the following relation:

$$F_{linkage} = \frac{F_{act}}{cos(\theta_{linkage})} \approx \frac{F_{act}}{cos(\theta_{act})} \tag{1}$$

As the linkage length will be much greater than arm length, $\theta_{linkage}$ can be approximated by θ_{act}.

Following the expression above, the actuator torque can be calculated as:

$$T_{act} = F_{linkage}cos(\theta_{linkage})r_{act} \tag{2}$$

In this expression, the r_{act} represents the torque arm length. The non-linear relationship between the actuator torque, T_{act} and the rotation angle, $\theta_{linkage}$ is reflected here by the cosine term. The next step was to find an optimal r_{act} to minimise the actuation loads at the required minimum travel of -5 to +7 mm. The analysis is shown above, and the kinematic model served as the basis for determining the latter parameter for the final actuator selection.

The static and dynamics requirement in terms of actuation force and stroke was to be determined from this analysis. As a dynamic bandwidth requirement, an actuation frequency of 1-2 Hz and $+/-40$ deg servo arm rotation, was determined. This was found sufficient to deal with required manoeuvre load alleviation objectives.

3.3 Aerodynamic Model

Aerodynamic behaviour is modelled using a strip model. At each FSI loop iteration, the deformed airfoil shape is sliced at discretised spanwise sections (31 in total) to extract a 2D deformed airfoil. The deformed airfoil shape is input to XFOIL [27], which calculates the pressure distribution over the deformed airfoil. This data is then used to calculate pressure loads to be applied
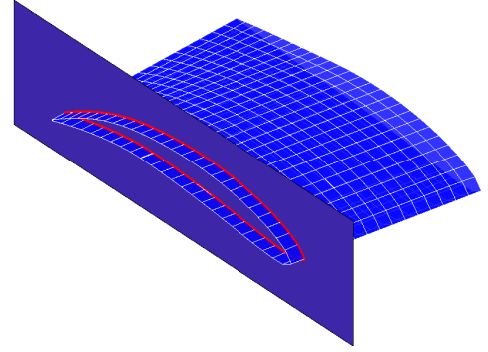

FIGURE 8: AIRFOIL SLICING ON THE DEFORMED FEM MESH

to the NASTRAN mesh. Slice planes coincide with NASTRAN grid points to limit the use of interpolation routines. This process of airfoil extraction is shown in Fig 8.

To calculate the pressure distribution with sufficient quality, additional mesh points were added onto the deformed airfoil. Specifically, to better represent the leading edge curvature and improve the resolution of the data on the morphing surface. This in-effect produces a higher resolution aerodynamic mesh, onto which pressure coefficients are mapped by interpolation. The difference in the structural and aerodynamic mesh is presented in Fig 9.
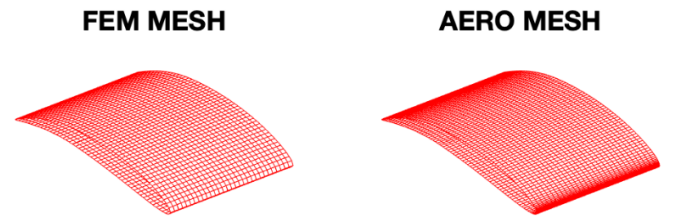

FIGURE 9: MESH COMPARISON FEM (LEFT) AND AERO (RIGHT).

3.4 System Coupling

As the meshes vary for the two models (i.e. the aerodynamic model has higher resolution), an interpolation routine must be used to transfer the aerodynamic-mesh $c_{p_{aero}}$ values to their ap-

propriate centroid location in the FEM- mesh $c_{p_{fem}}$ values. The interpolation function implements a gridded linear interpolation method based on Delaunay triangulation of the 2D grid data [28]. Since the interpolation is performed in 2D, the upper and lower pressure distributions of the airfoil are sampled from the aerodynamic mesh separately and projected independently onto the x, y projection of the FEM mesh, acting as x, y data sampling points for the interpolation. These sampling locations are the centroid of the mesh elements, as is illustrated in Fig 10. The interpola-
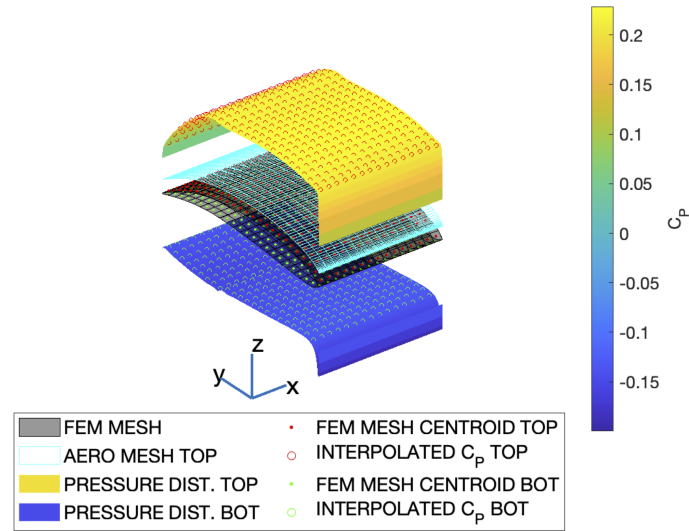

FIGURE 10: COUPLING OF DATA BETWEEN AERODYNAMIC AND FEM MODELS

tion method uses MATLAB's [29] *griddata* function. This function takes as input, the aerodynamic x, y grid sampling points, the $c_{p_{aero}}$ distribution, the desired FEM x, y grid sampling locations, and outputs the pressure the $c_{p_{fem}}$ distributions. Griddata is called twice for the upper and lower distribution. The interpolated pressure coefficients are then converted to pressure loads by evaluating the area of the corresponding mesh element. This is achieved using the NASTRAN PLOAD card [30], which allows evaluating static pressure load directly from pressure coefficients. Appropriate scaling must be applied with the airspeed for which the aerodynamic analysis was performed. The conversion from cp pressure to PLOAD pressure is performed as follows:

$$P_{PLOAD} = -c_{p_{fem}} 1/2 \rho V_\infty^2; \qquad (3)$$

The result of the interpolation routine can be visualised in Fig 10.

3.5 Verification

A key aspect in the FSI framework and in particular the system coupling between the FEM and aerodynamics was to determine (i) the required resolution of both meshes in order to eliminate discretisation effects due to the selected mesh density and (ii) convergence criteria for the model to exit the FSI loop.

3.5.1 Model Convergence To judge the convergence of the FSI system, the change in deformations was analysed at each iteration. To check for convergence, the change in the magnitude of deformation is calculated at each node. The sum of these differences represents the total deformation error of the system.

To find a suitable convergence bound, multiple analyses were run to a high iteration count. The change in lift coefficient and actuator input loads was monitored between each iteration in parallel to the deformation error. It was found that when the total deformation error of the system was below 0.01, the variation in the lift coefficient was less than 0.0001. With these negligible lift variations, the actuation loads stabilised to the nearest 0.001N, which was considered more than suitable for the accuracy of this analysis. For this reason, the convergence bound was set with a deformation error of 0.01, i.e. the simulation terminates once the deformation error ≤ 0.01.
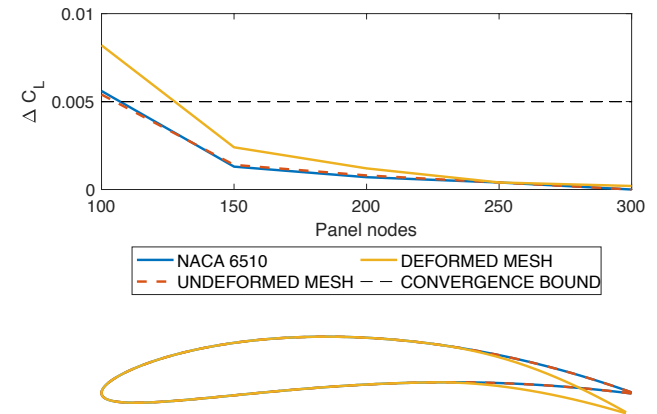

FIGURE 11: AERODYNAMIC MESH CONVERGENCE STUDY

3.5.2 Mesh Convergence FEM and aerodynamic mesh properties share implicit dependency due to data transfer taking place. The resolution of structural mesh defines the accuracy in the deformed structure and actuation loads. The resolution of the aerodynamic mesh, in turn, defines the accuracy of
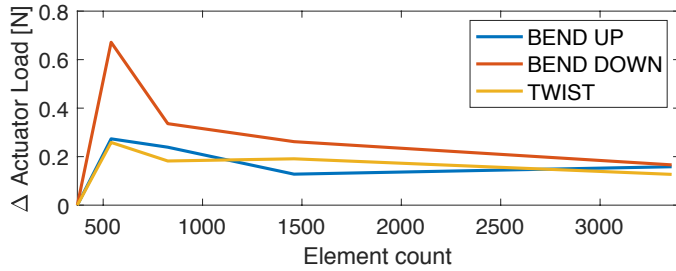
FIGURE 12: STRUCTURAL MESH CONVERGENCE STUDY

Subcase	CL_{linear} [−]	$CL_{non-linear}$ [−]
Bend up	-0.277	-0.296
Bend down	1.464	1.423
Twist	0.823	0.847
Unmorphed	0.825	0.825

TABLE 1: COMPARISON LINEAR VERSUS NON-LINEAR FEM MODEL FOR GIVEN DESIGN CASES

the pressure distribution. To determine a suitable combination of both, a mesh study was completed on both meshes.

Each mesh was refined separately in the study. Initially, a resolution of the aerodynamic mesh was evaluated. Then the aerodynamic mesh was fixed, and the structural mesh was refined to find a suitable structural mesh resolution.

Three morphing cases were analysed for the aerodynamic mesh study for the given base airfoil. These were, (i) the included NACA6510 in XFOIL, (ii) airfoil sliced from an un-deformed structural mesh, and (iii) airfoil sliced from a deformed structural mesh. Peak bend up (30mm), bend down (20mm), and twist (±20mm) were considered for the structural mesh study. The analysis was completed at zero angle-of-attack and velocity of 30 m/s.

Results of the mesh resolution studies are presented in Fig 11 and Fig 12. For both meshes, convergence was evaluated by tracking the ΔC_L value. The convergence of the actuator input load was also assessed for the structural mesh.

As observed from the figures, the aerodynamic mesh converged at 140 nodes. The XFOIL default node count of 160 nodes was maintained for future analyses. With this setting, the structural mesh converged beyond having 1500 elements. Due to the sufficiently quick run times, mesh resolution was increased to have a seed size of 10*mm* which resulted in an element count of 3360. This benefited it setting up design regions in 10*mm* increments on the morphing surface for improved optimisation.

3.6 Evaluation of Non-Linear Structural Effects

A further assessment was completed on the validity of a linear FEM model. Large deformations are present on the morphing surface, and as such, it needed to be verified if non-linear effects alter the results substantially. Therefore, a comparison between linear or non-linear solution in the FSI loop was completed. Peak bend up/down and twist cases were evaluated at zero angles of attack and wind speed of 30 *m/s*. Mesh densities were kept in accordance with the outcomes of the mesh convergence study.

Comparison of lift and actuator loads are presented in Tab. 1 for the two cases. The slight difference in deformations are presented in Fig 13. Although the deformation behaviour changes

slightly between the two solvers, the net performance does not substantially alter, and as such the linear assumption can be considered valid for the remainder of the design work.
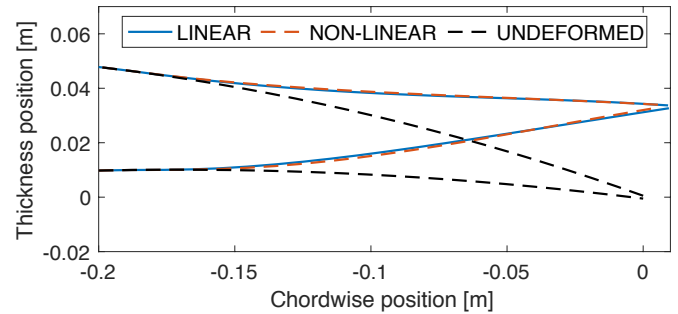

FIGURE 13: COMPARISON LINEAR VERSUS NON-LINEAR DEFORMATION FOR CASE BEND UP

3.7 Design Process Summary

The design process can be summarised as follows:

1. An optimisation routine which varied laminate thickness/ply orientation for the morphing surface was established using the FSI loop, to design a suitable laminate, needed to reach the defined target shapes at minimum input force.
2. The outputs of the optimisation were used to define an easy to manufacture laminate, which was further analysed to converge on the input loads and required actuator displacement. This data was used to select a suitable actuator.
3. The design was analysed on individual 300*mm* modules. The structure forward of the rear spar was modelled as rigid. A rigid wing box and the leading edge was designed to ensure each module operated similarly.
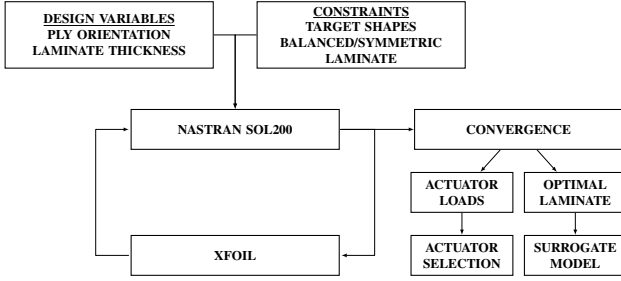
FIGURE 14: FLOW CHART OF THE FSI OPTIMISATION FRAMEWORK.

4 OPTIMISATION

The optimisation routine (shown in Fig. 14), was carried out with the NASTRAN's SOL200 optimiser [30] for the three morphing conditions defined in the previous section. These conditions were optimised *simultaneously* as a sub-cases in each optimisation run.

The integration of the optimisation routine in the entire design framework, presented in Fig. 14, shows how the SOL200 simulation is integrated into the FSI loop. The design variables and constraints serve as inputs to the SOL200 to achieve desired morphing shapes. The convergence of the system defines the optimal laminate and actuation loads. These outputs are used to select actuators and establish a surrogate model.

4.1 Input Parameters

The input parameters for the three sub-cases are listed in Tab. 2. The range of deformations listed in the table was chosen such that a ΔC_L of approximately 0.6 was achieved from baseline C_L at undeformed NACA6510 condition. A prior analysis was done to confirm the C_L increase, as shown in Tab. 1. The angles of attack were taken as acceptable design limits for operational use of a midsize UAV. The applied angle of attack was such that it opposed morphing action, thereby increasing the actuation loads. The difference in the selected angles of attack is due to the asymmetric shape of the baseline airfoil, which has a zero-lift angle of attack at -3.5deg.

The selected material for the design was Fibre Glass as it has a lower Young's modulus than Carbon-Fibre which would reduce actuation loads.

4.2 Design Parameters

Primary design constraints imposed were tip deflection, minimum skin thickness, equivalent to the ply thickness, and maximum allowable chordwise curvature. The latter being used to ensure a smooth airfoil shape without kinks. Additional constraints were introduced to help the optimiser find a solution, and these included maximum skin thicknesses (1.65mm, equivalent to the set wing box thickness) and allowable input load range.

TABLE 2: ANALYSIS SUB CASES

Subcase	TE Deformation [mm]	V_∞ [m/s]	Angle of Attack [°]
Bend up	30	30	−12
Bend down	−20	30	5
Twist	±20	30	0

The laminate was also constrained to be symmetric and balanced to evade bend-twist and extension-shear couplings.

The design variables which were considered for the optimisation routine were ply angle and laminate thickness distribution.

4.3 Optimisation Model

A trial and error approach was taken to find the suitable implementation of the design variables into the SOL200. The trials conducted in order included:

1. Trial 1: Optimisation of ply angle and laminate thickness for a variable thickness morphing surface
2. Trial 2: Optimisation of ply angle and laminate thickness for a constant thickness morphing surface
3. Trial 3: Optimisation of a variable thickness morphing surface with constant ply angle

The implementations and lessons learnt from each of these trials are further described in the following subsections.

4.3.1 Trial 1 The simultaneous optimisation of thickness distribution and ply angle proved to be difficult.

To achieve this, the morphing surface had to be sectioned off in discrete strips to allow for variable chordwise thickness distribution. The number of layers and the plies for each layer would be allowed to vary within each of these discretised strips.

With the considerable freedom allowed in design combinations, design constraints had to be introduced to ensure that the final laminate was balanced/symmetric and manufacturable.

Given the manufacturing technology (hand layup and impregnation) a manufacturable design was not possible to obtain, and therefore another approach was sought out.

4.3.2 Trial 2 The second approach undertaken was to constrain the thickness to be constant across the morphing surface. The design variables were still, the ply orientation and thickness, but discrete design strips were no longer required, which therefore reduced the number of possible design combinations significantly.

Design constraints were once again included in the model to ensure the final laminate was balanced and symmetric.

This approach showed converging results, but continually produced a laminate design with fibres always oriented in the spanwise direction. This, in effect, meant the chordwise strength of the laminate was defined by the strength of the matrix, which was too low and prone to cracking.

To overcome this problem, a higher minimum load constraint was introduced into the simulation. This forced the optimiser to place fibres off-axis to increase the stiffness of the system in the actuation direction.

The curvature of the morphed shapes was analysed, and it was seen that the airfoil shape did show minor kinks.

It was realised that tailoring ply drops, i.e. having a variable thickness in the chordwise direction would address the curvature limitations of this approach.

4.3.3 Trial 3 To be able to implement variable thickness distribution, the discrete strips had to be reintroduced into the optimiser. Due to the complications seen in trial 1, the ply orientation had to be fixed to reduce the number of design combinations. Various considerations were made to decide how to stack up a suitable laminate for this approach.

As demonstrated, the results from the previous trial, actuation force was minimised when the chordwise stiffness in the flap region was at a minimum, i.e. all fibres are oriented along the span of the wing. In this design, the chordwise strength is compromised. On the contrary, when all the fibres are oriented chordwise, the actuation force is at its highest. A balance is found in between.

$\pm 45°$ plies provide a compromise. Selection of this orientation also provided additional benefits:

1. They are available easily as woven plies. With each ply drop, the laminate remains symmetric balanced.
2. Lamination time is reduced as fewer layers need to be used.
3. Fibres are already correctly oriented.

With these considerations, the ply orientation was fixed to $\pm 45°$. Fibre-glass designation US 7630 (MIL-Y-1140H) was selected for use in the final design [31]. This latter approach presented the best results and was used to define the final laminate design.

5 VALIDATION AND RESULTS

To arrive at a final design, the optimisation routine described in Sec. 4 was performed for the sub-cases (Bend up, Bend down, and Twist) as described in Tab 2. This was used to generate the laminate design for the morphing concept. Furthermore, the FSI framework described in the design methodology in Sec. 3 was
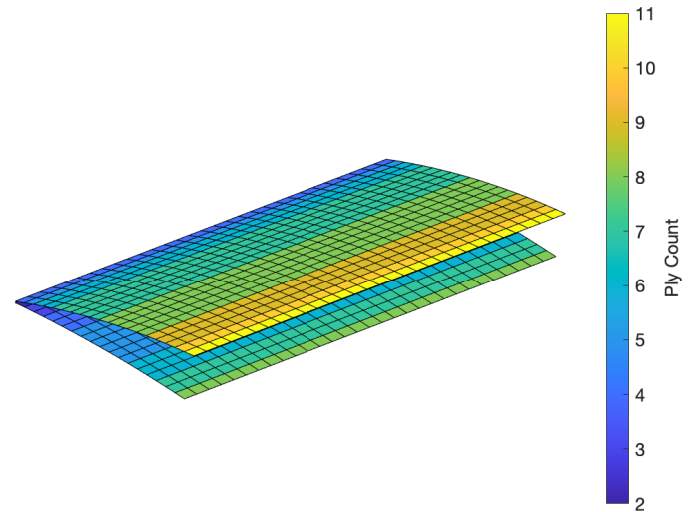

FIGURE 15: PLY DROPPING SEQUENCE

used to finalise the actuator design and prepare the work for the establishment of the surrogate model.

5.1 Laminate Design

During the optimisation process, a ply dropping sequence was determined. Fig 15 shows the undeformed morphing surface overlaid with the optimised thickness distribution. The colour map shows the number of plies required in each design region to build the morphing surface laminate.

The deformed morphing surfaces for the three sub-cases are presented in Fig 16. They are superimposed on an undeformed surface to visualise the degree of deformations taking place. The colours represent the relative vertical deformations of the system.

5.2 Actuator Loads

From the results of the optimisation routine, the peak actuation loads and the range of translation were determined. In Tab 3, the required input loads and horizontal travel for the three subcases are listed. The actuation load ranges from -60 to +61 N, with twist actuation made possible from asymmetric loads within this range. The translation range of the actuator ranges from -5 to +7 mm. The resulting lift coefficients range from -1.7 to + 2.2. This information aided in the selection of a suitable actuator for the application.

The travel range of free edge of the morphing surface is shown in Fig 17 for easier visualisation of the system.

With this information, the torque arm and rotation range ($\theta_{act,max}$) of the servo could be set in order to calculate torque requirements from the actuator. The actuator kinematic model was implemented according to the Free-Body Diagram illustrated in Fig 7.
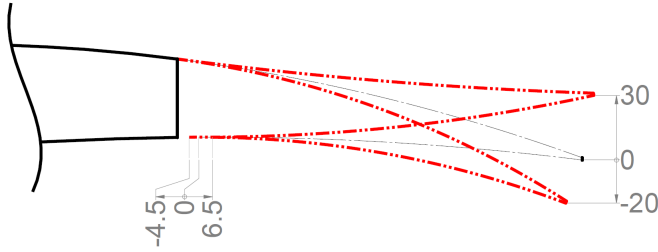
FIGURE 17: HORIZONTAL TRAVEL RANGE

FIGURE 18: LINKAGE FORCE AS A FUNCTION OF SERVO ROTATION

The approach is taken to design the kinematics was to minimise the torque arm, resulting in an increased available actuation force (F_{act}). This also resulted in an increase in the required range of rotation to cover the entire horizontal travel span. The range of rotation was limited to ensure linkage forces did not become substantially non-linear and allow for an operating margin to the full range of the servo. The relation of linkage force to $\theta_{act,max}$, defined by the Eq. 1, is presented in Fig 18.

Within this plot, it can be seen that the ratio of the linkage force relative to the actuator force rapidly moves further away from the 1:1 ratio beyond 40° of rotation. A higher linkage to actuator force ratio is beneficial in terms of actuation leverage. However, examining the Free-Body Diagram illustrated in Fig 7 it can be deduced that the higher ratio comes at the price, of reduced linear travel for higher rotation angles. To keep the rotation angle versus horizontal travel sensitivity at a reasonable level the rotation angle is limited to ±40°. For this range of rotation, the torque arm required for 7*mm* of horizontal travel was 10*mm*.

To determine the actuator torque requirements, the actuation loads were evaluated for the entire morphing range by incrementing horizontal travel at the actuation points, from -7mm to 7mm, in 1mm increments. Only symmetric actuation was considered
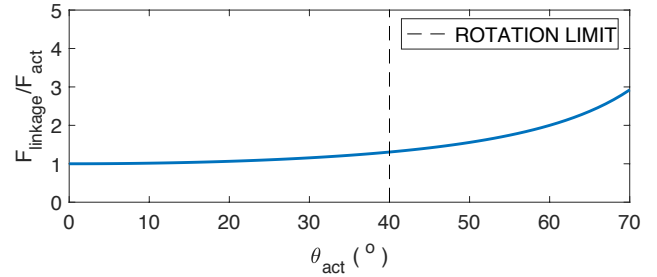
as loads were most adverse in this scenario. The analysis was conducted at 30 m/s. To ensure worst-case loads, the angle of attack was maintained at +5° for bend down cases and -12° for bend up cases. The data from these analyses are presented in Fig 19. It can be seen that torque increases in a non-linear fashion, with peak torque requirements being 0.45 Nm for bend up, and -0.6 Nm for bend down. At zero travel, the lines do not coincide as the analyses for the two cases were done at two different angles of attack.

For the peak loads presented in Tab 3, the peak torque required to actuate all morphing shapes at $V_\infty = 30$ m/s is ±0.6 Nm. To account for higher loads, free-stream velocities, increased camber, and higher angles-of-attack. A design safety margin was established to account for higher free-stream velocities, increased camber, and higher angles-of-attack. This was established in the form of an operational safety margin of ≈ 35% resulting in peak torque of ±0.8 N.m. at $V_\infty = 50$. was established

Furthermore, based discussion in Sec. 3, a dynamic bandwidth requirement, of 1-2 Hz actuation frequency at +/−40 deg servo arm rotation, was set to cope with active manoeuvre load alleviation task. This target requirements can be visualised as a
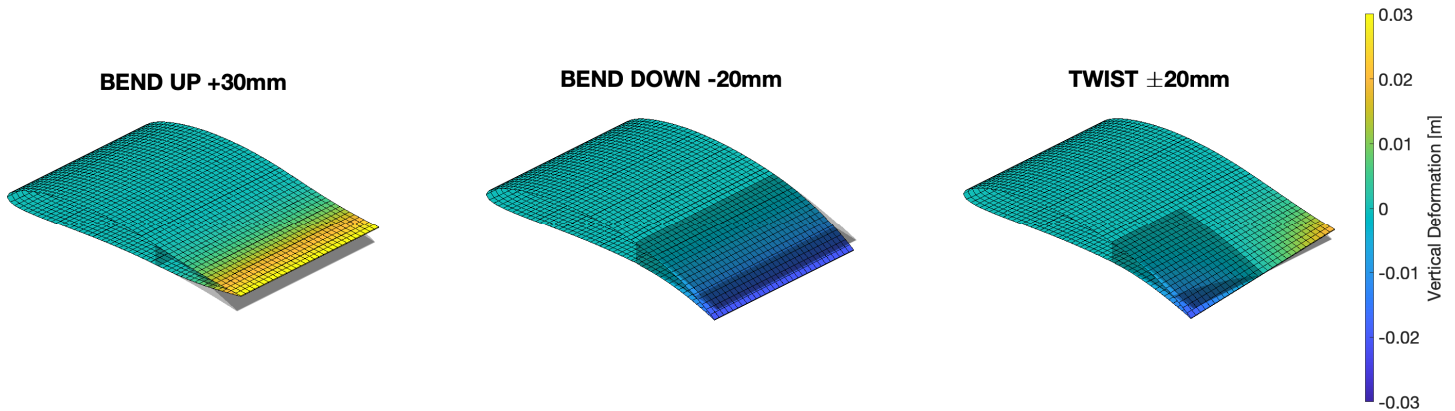

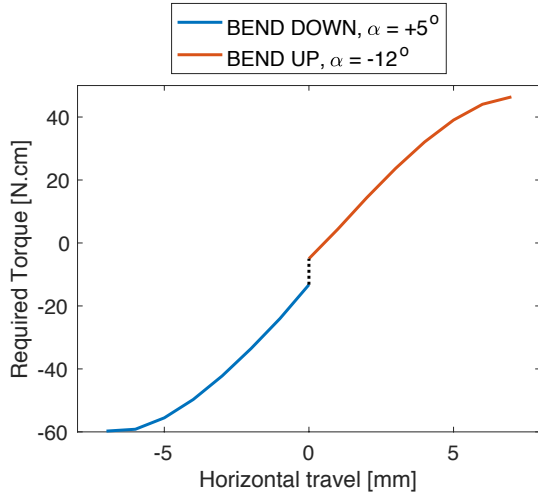**FIGURE 16**: DEFORMED MORPHING SURFACES FOR ALL SUB CASES

FIGURE 19: TORQUE VERSUS HORIZONTAL TRAVEL, BEND DOWN AND BEND UP CONSIDERED

FIGURE 20: VOLZ DA-22-12-4112 PERFORMANCE PARAMETERS [32]

repeating triangular ramp signal, with amplitudes of $+-40\,\mathrm{deg}$ servo rotation to be completed continuously withing the required bandwidth frequency. Consequently, the requirement for the actuator was the following:

1. capability to deliver a peak torque of at least ± 0.8 Nm
2. ability to operate this peak toque continuously at 1-2 Hz at $+/-40\,\mathrm{deg}$ servo arm rotation

With these two requirements, various actuators were analysed. The selection was made between the available actuator models of the servo manufacturer Volz [32]. The reason this supplier was chosen was due to the real-time actuator position feedback. Volz DA 22-12-4112 was selected to be the most suitable for the application. Fig. 20 shows the performance specification data of the actuator published by the manufacturer [32]. The green region indicates the continuously operational range of the servo. As seen, the peak torque requirement, indicated with a red-dotted box, falls within the continuous operation range of the servo.

5.3 Surrogate Model

Preparation work was done for the construction of the surrogate model, and it was concluded that more investigations were necessary to determine additional non-linearities that may be present in the morphing model and the required network structure. As an initial setup, the input was considered to be the actuator displacements (1,2) and the angle of attack. The main focus of the surrogate model was to obtain the change in lift, drag and moment coefficients, $\Delta C_L, \Delta C_D, \Delta C_M$, and from these their respective control effectiveness derivatives. A Deep Neural Network (DNN) network structure with three inputs, a hidden
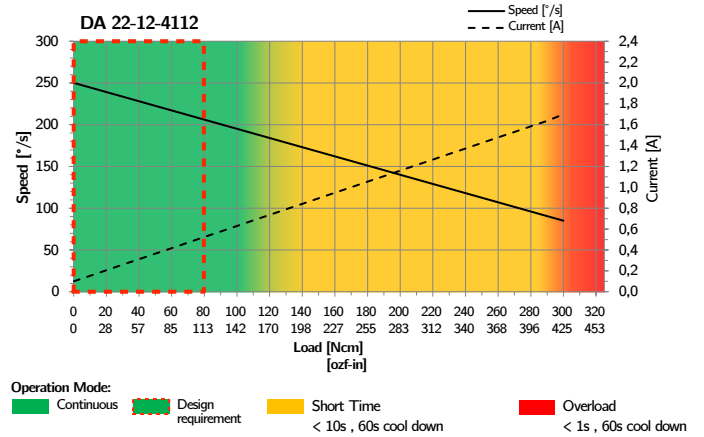
TABLE 3: ACTUATOR PEAK FORCES FOR VARIOUS SUBCASES

Subcase	Act1 Force [N]	Act2 Force [N]	Act1 Disp. [mm]	Act2 Disp. [mm]	C_L
Bend up	61	61	6.5	6.5	-1.7
Bend down	-60	-60	-4.5	-4.5	2.2
Twist	-50	23	4.5	-4.5	0.85

sigmoid layer and an output layer was considered with varying neurons (15-150) in terms of approximation accuracy. Investigations on test data showed good results of approximating the aerodynamic dataset of a fighter aircraft [33].

Initial investigations into the lift response are presented in Fig. 21. The data presented was determined through the FSI analysis of a single wing module at a speed of 30 m/s. The actuator inputs were incremented in 2mm increments, from -4mm to +4mm, with a C_L recorded for each analysis. The data shows a highly linear response between lift and actuator inputs. This trend suggests that the control effectiveness derivatives can be represented as coefficients, and a control gain scheduling scheme could be used to cover the given operational range of the model. However, the initial FSI analysis was restricted to a single module; hence further investigation is required to verify the results for the full operational range of the entire wing. These are still ongoing.
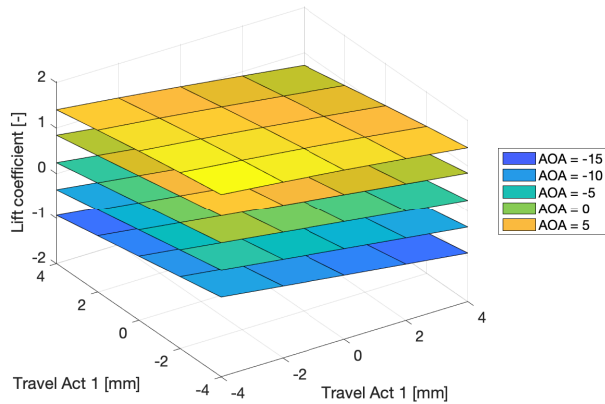
FIGURE 21: LIFT RESPONSE FOR VARYING ACTUATOR INPUTS AND ANGLE OF ATTACK (AOA)

6 CONCLUSION AND RECOMMENDATION

In this study, the design and development of an autonomous morphing wing concept were presented. A novel distributed morphing concept was proposed, with six TRIC morphing trailing edge modules, interconnected with triangular flexible skin segments to allow seamless variation of local lift distribution along the wingspan, therewith addressing the drawbacks of the existing TRIC morphing concept. The main advantage of the design was that the modular design allowed independent camber and twist distribution, to control lift distribution along the span of the wing. This way, the performance of the wing could be optimised for the most optimal lift to drag ratio (shape control) to minimise drag. Additionally, the lift distribution can be adapted to perform manoeuvre load alleviation when necessary. Lastly, fast piezoelectric actuators were envisioned to be implemented in the trailing for aeroelastic control and drag minimisation. Further work is in planning to investigate the design and effectiveness discuss of the piezoelectric actuators.

An FSI structural optimisation tool was developed with NASTRAN and XFOIL to (i) produce the optimised morphing design and (ii) build a surrogate model of the morphing system for use in active control methodology. The primary outcome of the FSI analysis and optimisation was to an optimal laminate design, in terms of laminate thickness at pre-defined ply orientations, capable of reaching target shapes and minimise actuation loads. Fibre Glass weave (-+/-45 degree orientation) was chosen as the laminate material, due to its availability, ease of manufacturing and low stiffness properties relative to carbon fibre.

Furthermore, based on the analysis of the kinematic model of the embedded actuator, Volz DA-22-12-4112 22mm class servo was selected [32]. The actuator was selected based on its capability to deliver the actuation loads in continuous operational mode and fulfil both static and dynamic requirements in terms of bandwidth, actuation force and stroke.

Finally, an initial surrogate model of a single module was constructed holding the input-output mapping of the actuator horizontal travel input, angle of attack and the resulting lift increments. As a part of the future work, Deep Neural Network (DNN) was considered for approximating the input-output mapping for the remaining control effectiveness derivatives of a full wing

Preparations were made in this study for the next stage of the Smart-X design, to build a functional demonstrator and obtain a surrogate-based control to derive the control laws. The demonstrator will be tested in the wind tunnel facilities at the Delft University of Technology, where both static and dynamic loads, as well as the real-time drag, will be measured to assess the objectives defined in the Smart-X project.

REFERENCES

[1] Lentink, D., Müller, U. K., Stamhuis, E. J., De Kat, R., Van Gestel, W., Veldhuis, L. L., Henningsson, P., Hedenström, A., Videler, J. J., and Van Leeuwen, J. L., 2007. "How swifts control their glide performance with morphing wings". *Nature,* **446**(7139), pp. 1082–1085.

[2] Bomphrey, R. J., Henningsson, P., and Hedenstro, A., 2014. "Efficiency of Lift Production in Flapping and Gliding Flight of Swifts". *PLoS ONE,* **9**(2).

[3] JEX, H., and CULICK, F., 1985. "Flight control dynamics of the 1903 Wright Flyer". In 12th Atmospheric Flight Mechanics Conference, American Institute of Aeronautics and Astronautics.

[4] Weisshaar, T. A., 2013. "Morphing aircraft systems: Historical perspectives and future challenges". *Journal of Aircraft,* **50**(2), mar, pp. 337–353.

[5] Barbarino, S., Bilgen, O., Ajaj, R. M. R., Friswell, M. M. I., and Inman, D. D. J., 2011. "A review of morphing aircraft". *Journal of Intelligent Material Systems and Structures,* **22**(9), jun, pp. 823–877.

[6] Kintscher, M., Geier, S., Monner, H. P., and Wiedemann, M., 2014. "Investigation of multi-material laminates for smart droop nose devices". *29th Congress of the International Council of the Aeronautical Sciences, ICAS 2014*, pp. 1–11.

[7] Sodja, J., Martinez, M. J., Simpson, J. C., and De Breuker, R., 2019. "Experimental evaluation of a morphing leading edge concept". *Journal of Intelligent Material Systems and Structures,* **30**(18-19), pp. 2953–2969.

[8] Vasista, S., De Gaspari, A., Ricci, S., Riemenschneider, J., Monner, H. P., and Van De Kamp, B., 2016. "Compliant structures-based wing and wingtip morphing devices". *Aircraft Engineering and Aerospace Technology, 88*(2), mar, pp. 311–330.

[9] Previtali, F., Arrieta, A. F. A., and Ermanni, P., 2014. "Performance of a Three-Dimensional Morphing Wing and Comparison with a Conventional Wing". *AIAA Journal, 52*(10), oct, pp. 2101–2113.

[10] Molinari, G., Quack, M., Arrieta, A., Morari, M., and Ermanni, P., 2015. "Design, realization and structural testing of a compliant adaptable wing". *Smart Materials and Structures, 24*(10).

[11] Previtali, F., and Ermanni, P., 2012. "Performance of a non-tapered 3D morphing wing with integrated compliant ribs". *Smart Materials and Structures, 21*(5).

[12] Molinari, G., Arrieta, A., and Ermanni, P., 2014. "Aero-structural optimization of three-dimensional adaptive wings with embedded smart actuators". *AIAA Journal, 52*(9), pp. 1940–1951.

[13] Woods, B., Dayyani, I., and Friswell, M., 2015. "Fluid/structure-interaction analysis of the fish-bone-active-camber morphing concept". *Journal of Aircraft, 52*(1), pp. 307–319.

[14] Woods, B., Bilgen, O., and Friswell, M., 2014. "Wind tunnel testing of the fish bone active camber morphing concept". *Journal of Intelligent Material Systems and Structures, 25*(7), pp. 772–785.

[15] Woods, B., Friswell, M., and Wereley, N., 2014. "Advanced kinematic tailoring for morphing aircraft actuation". *AIAA Journal, 52*(4), pp. 788–798.

[16] Kota, S., Hetrick, J. A., Osborn, R., Paul, D., Pendleton, E., Flick, P., and Tilmann, C., 2003. "Design and application of compliant mechanisms for morphing aircraft structures". In Smart Structures and Materials 2003: Industrial and Commercial Applications of Smart Structures Technologies, E. H. Anderson, ed., Vol. 5054, SPIE, p. 24.

[17] Kota, S., Flick, P., and Collier, F., 2016. "Flight testing of the FlexFloil^TM adaptive compliant trailing edge". *54th AIAA Aerospace Sciences Meeting*.

[18] Cramer, N. B., Cellucci, D. W., Formoso, O. B., Gregg, C. E., Jenett, B. E., Kim, J. H., Lendraitis, M., Swei, S. S., Trinh, G. T., Trinh, K. V., and Cheung, K. C., 2019. "Elastic shape morphing of ultralight structures by programmable assembly". *Smart Materials and Structures, 28*(5), apr, p. 055006.

[19] Jenett, B., Calisch, S., Cellucci, D., Cramer, N., Gershenfeld, N., Swei, S., and Cheung, K. C., 2017. "Digital Morphing Wing: Active Wing Shaping Concept Using Composite Lattice-Based Cellular Structures". *Soft Robotics, 4*(1), mar, pp. 33–48.

[20] Bilgen, O., and Friswell, M., 2014. "Piezoceramic compos-

[21] Bilgen, O., Butt, L., Day, S., Sossi, C., Weaver, J., Wolek, A., Mason, W., and Inman, D., 2013. "A novel unmanned aircraft with solid-state control surfaces: Analysis and flight demonstration". *Journal of Intelligent Material Systems and Structures, 24*(2), pp. 147–167.

[22] Pankonien, A., Faria, C., and Inman, D., 2015. "Synergistic smart morphing aileron: Experimental quasi-static performance characterization". *Journal of Intelligent Material Systems and Structures, 26*(10), pp. 1179–1190.

[23] Mistry, M., and Gandhi, F., 2015. "Design, fabrication, and benchtop testing of a helicopter rotor blade section with warp-induced spanwise camber variation". *Journal of Intelligent Material Systems and Structures, 26*(10), pp. 1272–1289.

[24] Werter, N. P., Sodja, J., Spirlet, G., and De Breuker, R., 2016. "Design and experiments of a warp induced camber and twist morphing leading and trailing edge device". *24th AIAA/AHS Adaptive Structures Conference*.

[25] Vos, R., Gürdal, Z., and Abdalla, M., 2010. "Mechanism for warp-controlled twist of a morphing wing". *Journal of Aircraft, 47*(2), pp. 450–457.

[26] Rodden, W. P., and Johnson, E. H., 1994. *MSC/NASTRAN aeroelastic analysis: user's guide; Version 68*. MacNeal-Schwendler Corporation.

[27] Drela, M., 1989. *XFOIL: an analysis and design system for low Reynolds number airfoils.* No. 54), Berlin, Germany, Springer-Verlag, 1989. Springer-Verlag Wien.

[28] Watson, D. F., 1992. "Contouring: a guide to the analysis and display of spatial data". *Contouring: a guide to the analysis and display of spatial data*.

[29] MATLAB, 2019. *MATLAB version 9.6.0.1072779 (R2019a)*. The Mathworks, Inc., Natick, Massachusetts.

[30] MSC Nastran, 2001. MSC Nastran 2012 Design Sensitivity and Optimization User's Guide Main Index. Tech. rep., MSC Nastran.

[31] Interglas, 2010. Glass Filament Fabrics for Plastics Reinforcement - 92110 Product Specification. Tech. Rep. 0, Interglas.

[32] Volz, 2013. Volz DA 22 Actuator Technical Specification. Tech. rep., Volz Servos GmbH.

[33] Nguyen, L. T., Ogburn, M. E., Gilbert, W. P., Kibler, K. S., Brown, P. W., and Deal, P. L., 1979. Simulator Study of Stall/Post-Stall Characteristics of a Fighter Airplane With Relaxed Longitudinal Static Stability. Tech. rep., NASA.